Proceedings of the 7th International Symposium on Cavitation
CAV2009
August 17-22, 2009, Ann Arbor, Michigan, USA

NUMERICAL STUDY OF VORTEX CAVITATION SUPRESSION WITH POLYMER INJECTION

Quan Zhang
DYNAFLOW INC.
Jessup, MD - 20794
quan@dynaflow-inc.com

Chao-Tsung Hsiao
DYNAFLOW INC.
Jessup, MD - 20794
ctsung@dynaflow-inc.com

Georges Chahine
DYNAFLOW INC.
Jessup, MD - 20794
glchahine@dynaflow-inc.com

ABSTRACT

A FENE-P model was implemented in the Navier-Stokes solver, 3DYNAFS-VIS, to simulate polymer solutions viscoelastic effects on tip vortex cavitation. Two problems encountered in tip vortex cavitation dynamics were studied numerically. The first problem is that of bubble growth/collapse in a line vortex. The second problem is that of the dynamics a propeller tip vortex in water and in polymer solutions. Bubble growth/collapse in the polymer solution was found to have a shorter period and smaller volume oscillation amplitude than in water. The bubble shape also differs from that in water.. Concerning the propeller flow, a RANS solution was first obtained for the full flow field, and then improved by conducting direct Navier Stokes simulations within a reduced domain encompassing the tip vortex with a much finer grid mesh. The viscoelastic effects were only considered in the reduced domain, which is an approximation of the case of local polymer injection such as from the propeller tip. The pressure along the vortex centerline was found to be higher for the polymer solution than for water. The maximum tangential velocity along the vortex for polymer solutions was found to be reduced, and the axial velocity component increased. In the two problems investigated, the presence of polymer makes cavitation more difficult to occur, which is consistent with the experimental observations.

INTRODUCTION

Great efforts have been devoted to the reduction of the tip vortex cavitation (TVC) and different approaches have been investigated. Among these methods, it was found that TVC can be efficiently delayed by injecting dilute polymer solutions from the blade tip. Fruman and Aflalo [1] reported that for an elliptic hydrofoil, the injection of the polymer solution increases the tip vortex radius as well as reduces the tangential velocity. Chahine *et. al* (1993) [2] investigated the TVC for a rotating propeller with the injection of Polyox WSR301 solutions as well as water/glycerin mixtures. They found that the cavitation inception number can be decreased by as much as 35% with polymer injection, while under the same conditions a water/glycerin mixture does not affect the inception characteristics. The different performances of the polymer solution and Newtonian fluid were confirmed later by Fruman *et. al* (1995) [3]. These results imply that the viscoelastic properties of the Polyox solution injected into the vortex core is responsible for the difference. Latorre *et. al* (2004) [4] carried out a theoretical analysis of TVC inception based the Rankine vortex model. In their analysis, the bubbles were assumed to be spherical and the non-Newtonian features of the polymer solution were assumed to only affect the vortex core radius.

It should be noted that most existing studies of TVC were focused on experiments, which unfortunately could not provide the details of the flow-structure modification due to the polymers as those structures are so small that it is extremely difficult to measure them accurately. Also, the non-Newtonian features of a polymer solution involve many aspects, such as shear-thinning effect, stretching-induced normal stress effect, etc. and the measurement of the polymer stresses is even harder than that of the flow structures. Since previous researchers have built up models accounting for these effects (see e.g. [5]), numerical approaches to model viscoelasticity have been adopted more and more to study the polymeric flows. In this study, we implement and use such a method to investigate the polymer effects on bubble growth and collapse in a vortex flow and the tip vortex flow of a propeller.

GOVERNING EQUATIONS

The flow of a dilute, homogeneous and incompressible polymer solution is described by the continuity and the momentum conservation momentum equations:

$$\nabla \bullet \mathbf{u} = 0, \tag{1}$$

$$\frac{D\mathbf{u}}{Dt} = -\nabla p + \frac{\beta}{\mathrm{Re}}\nabla^2 \mathbf{u} + \frac{1-\beta}{\mathrm{Re}}\nabla \bullet \mathbf{T}. \tag{2}$$

In the equations above, $\mathbf{u}$ represents the fluid velocity, p the pressure, t the time, and $\mathbf{T}$ the viscoelastic extra-stress tensor. Equations (1) and (2) are in a non-dimensional form with a

characteristic velocity, U, and characteristic length, l. The Reynolds number, R_e, is based on U, l and the total viscosity, $\mu = \mu_s + \mu_p$, where μ_s is the solvent (water) viscosity and μ_p the extra shear viscosity due to the polymer. The parameter β can be regarded as the viscosity portion due to the solvent

$$\beta = \frac{\mu_s}{\mu}. \tag{3}$$

The polymer stress is non-dimensionalized with $\mu_p \frac{U}{l}$.

The polymer stress tensor $\mathbf{T}$ is related to the flow field strains through the constitutive equation of the Finitely Extensible Nonlinear Elastic-Peterline) (FENE-P) dumbbell model [5]:

$$\mathbf{T} = \frac{1}{D_e}\left(f\mathbf{c} - a\mathbf{I} \right), \tag{4}$$

where $\mathbf{c}$ is the conformation tensor, defined as the ensemble averaged dyad of the end-to-end distance of the polymer chains. D_e is the Deborah (or Weissenberg) number, which is the non-dimensional relaxation time λ of the polymer

$$D_e = \frac{\lambda}{l/U}, \tag{5}$$

and f is the Peterlin function

$$f = \frac{L^2}{L^2 - c_{kk}}, \tag{6}$$

where L is the extensibility parameter and c_{kk} is the trace of tensor $\mathbf{c}$.

The equation for the conformation tensor $\mathbf{c}$ is governed by

$$\frac{D\mathbf{c}}{Dt} - \left(\nabla\mathbf{u} \bullet \mathbf{c} + \mathbf{c} \bullet \nabla\mathbf{u}^T \right) = -\frac{1}{De}\left(f\mathbf{c} - a\mathbf{I} \right), \tag{7}$$

in which the superscript 'T' denotes the transpose . The parameter a depends on L as follows,

$$a = \frac{1}{1 - \frac{3}{L^2}}. \tag{8}$$

When $L \to \infty$, FENE-P model recovers the Oldroyd-B model. In this study, L is set to be 60.0, as used in Ref. [6].

NUMERICAL METHOD

As seen in the previous section, the polymer stress in the momentum equation (2), depends on the velocity field via equation (7). Solution of the fully coupled system is complex. However, if the solution of the constitutive and momentum equations are staggered, i.e. the polymer contribution in equation (2) is calculated st each step once the velocity is known, then equation (2) can be solved as the usual Navier-Stokes equation with a body force term from the divergence of the polymer stress. A similar idea was implemented in other studies (see e.g.[7]).

At time step n, the velocity $\mathbf{u}^n$, the pressure p^n, and the polymer stress $\mathbf{T}^n$ are known. Based on $\mathbf{u}^n$, Equation (7) can be integrated to provide the conformation tensor for the next time step. A first order in the time stepping scheme is used in this study:

$$\frac{\mathbf{c}^{n+1} - \mathbf{c}^n}{\Delta t} = \left[-\mathbf{u} \bullet \nabla\mathbf{c} - \left(\nabla\mathbf{u} \bullet \mathbf{c} + \mathbf{c} \bullet \nabla\mathbf{u}^T \right) - \frac{1}{De}\left(f\mathbf{c} - a\mathbf{I} \right) \right]^n, \tag{9}$$

where Δt is the time step.

For the spatial discretization of Equation (9), a first order upwind scheme is used for the convection term and a second order center difference scheme is used for the velocity gradient. After obtaining $\mathbf{c}^{n+1}$, the polymer stress $\mathbf{T}^{n+1}$ is calculated from Equation (4) and the divergence of $\mathbf{T}$ is obtained. This provides the polymer stress term in equation (2)

$$\mathbf{b}_{polymer} = \frac{1-\beta}{\mathrm{Re}} \nabla \mathbf{g}\mathbf{T}^{n+1}, \tag{10}$$

and the momentum equation at step n+1 becomes:

$$\frac{D\mathbf{u}^{n+1}}{Dt} = -\nabla p^{n+1} + \frac{\beta}{\mathrm{Re}} \nabla^2 \mathbf{u}^{n+1} + \mathbf{b}_{polymer}, \tag{11}$$

which has the same form as the Newtonian Navier-Stokes equation.

Together with the continuity equation, Equation (11) is solved to get the velocity $\mathbf{u}^{n+1}$ and the pressure p^{n+1}. At this point, all the quantities for step n+1 are known and a new loop starts with the calculation of $\mathbf{c}^{n+2}$.

To simulate propeller and moving free surfaces flows, a boundary-fitted curvilinear grid is generated and Equations(1), (2) and (7) were transformed into a general curvilinear coordinate system and implemented in DYNAFLOW's flow solver 3DYNAFS-VIS. 3DYNAFS-VIS has evolved from its previous version, DF_UNCLE, and now includes the present viscoelastic model an Eulerian/Lagrangian two-way coupling scheme for simulation of bubble/liquid two phase flows and a Level Set method for simulation of large-deformation free surface flows.

3DYNAFS-VIS is based on the artificial-compressibility method [8], in which an artificial time derivative of the pressure is added to the continuity equation as

$$\frac{1}{\beta_c}\frac{\partial p}{\partial t} + \nabla \bullet \mathbf{u} = 0, \tag{12}$$

where β_c is the artificial compressibility factor. As a consequence, the hyperbolic system of equations (1) and (2) is formed (if accounting for the polymer stress contribution is done in a staggered fashion as explained above) and is solved using a time marching scheme in the pseudo-time to reach a steady-state solution. To obtain a time-dependent solution, a Newton iterative procedure is performed in each physical time step in order to satisfy the continuity equation.

The numerical scheme in 3DYNAFS-VIS uses a finite volume formulation. A first-order Euler implicit difference formula is applied to the time derivatives. The spatial differencing of the convective terms uses the flux-difference splitting scheme based on Roe's method [9] and a van Leer's MUSCL method for obtaining the first- or third-order fluxes. A second-order central differencing is used for the viscous terms which are simplified using the thin-layer approximation. The flux Jacobians required in an implicit scheme are obtained numerically. The resulting system of algebraic equations is solved using a Discretized Newton Relaxation method in which

symmetric block Gauss-Seidel sub-iterations are performed before the solution is updated at each Newton interaction.

RESULTS

Polymer solutions viscosity and relaxation time

To simulate the flow , the viscosity and relaxation time of the polymer solution are needed for different polymer concentrations. Since, in experimental studies of TVC suppression, Polyox WSR301 is widely used, we measured the total shear viscosity of Polyox solutions at different concentrations using the falling-ball method. Figure 1 shows the total shear viscosity at different polymer concentrations. Rigorously speaking, the falling –ball method is only applicable to a Newtonian fluid, however, as pointed out by Chhabra *"…The limited experimental evidence suggests that in the case of shear-thinning viscoelastic fluids, the drag on a sphere is largely determined by the shear dependent viscosity and that the viscoelasticity appears to exert little influence at least for small values of Weissenberg (Deborah) number…"* [10].

The relaxation time of Polyox WSR301 has been reported by Lindner *et. al* [11] in their table 1.

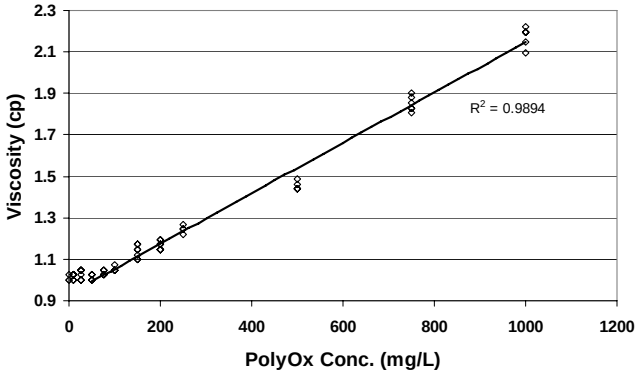

Figure 1. Shear viscosity of Polyox WSR301 solution at different concentrations

Initial radius(μm)	*Polymer concentration(ppm)*	R_e	D_e	β
100	0	70000	0	1.0
10	500	46667	10	0.667
	1000	35000	10	0.5

Table 1: Parameters used in the simulations of bubble growth and collapse in a vortex line.

Bubble dynamics in a line vortex

Bubble growth/collapse in a line vortex in water has been investigated by Hsiao & Chahine (2001) [12] and Choi *et. al* (2009) [13] using the same present computational method. In this section, we present the effect of a polymer solution on the results. For simplicity, a Rankine-like model is used.

Let a_c be the vortex core radius, Γ the vortex circulation, and r the distance of a field point to the vortex axis. The characteristic length, velocity and are chosen to be

$$l = a_c \qquad U = \frac{\Gamma}{2\pi a_c}. \tag{13}$$

In the numerical simulations, the vortex parameters are chosen to be a_c = 0.00508 m and Γ = 0.4398 m^2/s.

The non-dimensional velocity for a Rankine vortex is

$$\mathbf{u} = \begin{cases} \dfrac{1}{r^*}\mathbf{e}_\theta, & r^* \geq 1, \\ r^*\mathbf{e}_\theta, & r^* < 1, \end{cases} \tag{14}$$

where the superscript '*' denotes a dimensionless quantity and $\mathbf{e}_\theta$ is the azimuthal unit vector. Consider a similar model in a polymer solution: the viscous core undergoes rigid-body rotation, whereas outside the core, the velocity is determined by Equations (1) and (2). Due to shear-thinning effects, the azimuthal velocity is different from that shown in (14) but for large r, as the shear rate decreases, the velocity still approaches the $1/r*$ trend asymptotically. The simulation is to mimic the capture of a bubble nucleus by the vortex.

To obtain the steady solution of the vortex (velocity, pressure, and polymer stress) before introduction of the bubble Equations (1) and (2) are solved. The velocity profiles for water and a polymer solution are shown in Figure 2. We can see the velocity for the polymer solution is slightly different from that of water (Newtonian).

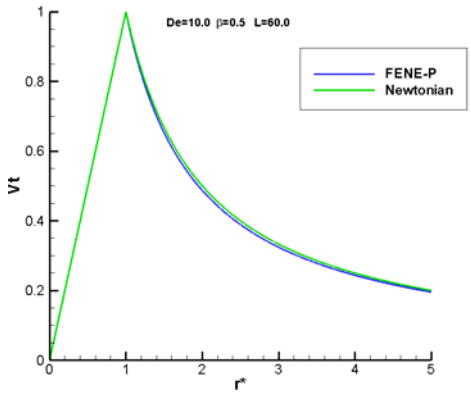

Figure 2. Initial non-dimensional velocity profile for the line vortex in water and in a viscoelastic liquid.

We then considered a bubble, which has an initial radius, R_0 and an internal pressure $p_{initial}$. The bubble is selected to be at equilibrium with the pressure at infinity p_∞, i.e.

$$p_{initial} - p_\infty = \frac{2\gamma}{R_0}, \tag{15}$$

where γ is the surface tension parameter. The cavitation number

$$\sigma = \frac{p_\infty - p_v}{\frac{1}{2}\rho U^2} \tag{16}$$

for this study is 1.9, in which p_v is the water vapor pressure. The bubble is initially placed at the vortex center and the simulation starts with an initial condition which is constructed by superposing the flow due to the bubble dynamics solution from the Rayleigh-Plesset equation and the original Rankine vortex flow field. The detailed setup of the initial condition can be found in Refs. [13] and [14].

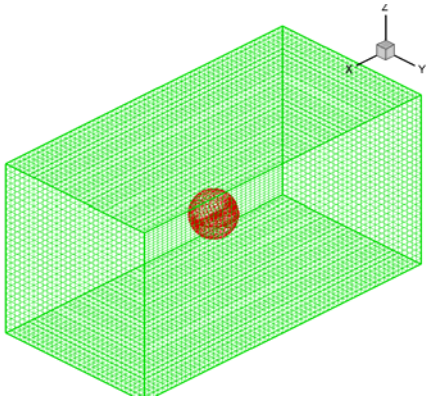

Figure 3. Overset grid system used in the simulations of a bubble in a vortex.

To simulate the bubble dynamics in the line vortex, a moving overset grid scheme is used as shown in Figure 3. A total of 41×21×21 grid points are used to generate the spherical sub-grid for the bubble, with 41×21 grid nodes used on the bubble surface. This sub-grid adapts to the motion of the bubble and is overset onto a rectangular background grid which has a total of 61×31×31 grid points. Two concentrations, 500 and 1000ppm of Polyox WSR301 were simulated. As reported in [11], the relaxation time for 500 and 1000ppm Polyox WSR301 are both about 0.0039s so that the Deborah numbers for both concentrations are about 10. The Reynolds number for the considered vortex flow in the case of water is 70,000. As shown in Figure 1, the viscosity approximately increases linearly with the concentration and $\mu_{500\,ppm} \approx 1.5\mu_{water}$, $\mu_{1000\,ppm} \approx 2.0\mu_{water}$. Since the density for the polymer solution differs little from that of water, the Reynolds numbers for the two Polyox concentrations are about 46,670 and 35,000 respectively. The parameters for the simulations are summarized in Table 1.

Figure 4 shows snapshots of the bubble evolution in time for a bubble of initial radius 100μm in water. During the initial phase of the bubble growth, the bubble grows almost spherically. Later on, the bubble shape starts to depart from spherical. First the bubble elongates and it then becomes peanut-like and starts to shrink and becomes spindle-like and finally splits into two sub-bubbles.

Figure 5 shows similar snapshots for the same bubble of initial radius 100μm but in the 500ppm Polyox WSR301 solution. Initially, like in water, the bubble grows almost spherically but after reaching its maximal volume, the bubble deviates less from a spherical shape during its collapse and the peanut and spindle-like shapes are delayed.

As shown in Figure 6, the bubble growth/collapse in the 1000ppm Polyox solution behaves in a similar pattern as that in the 500ppm solution, and the delay in shape deformation is greater. As a result, the final bubble volume before splitting is smaller than in the 500ppm case. Figure 7 shows the final bubble shapes for water, 500 and 1000ppm polymer solutions using the same length scale. The final bubble volume in water is much larger than those in the polymer solutions and as the concentration increases, the bubble volume decreases.

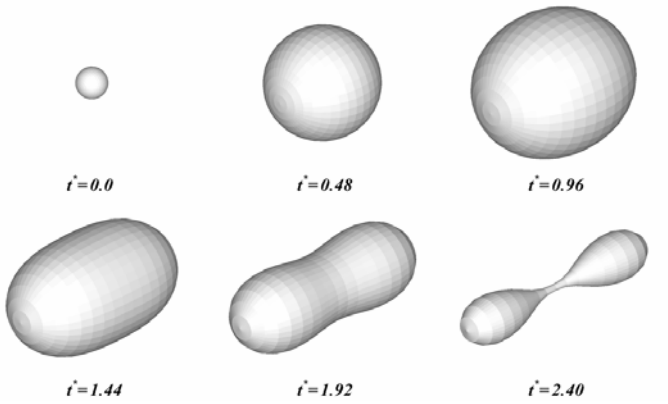

Figure 4. Bubble shape evolution in water for R_0 = 100μm, R_e=70,000.

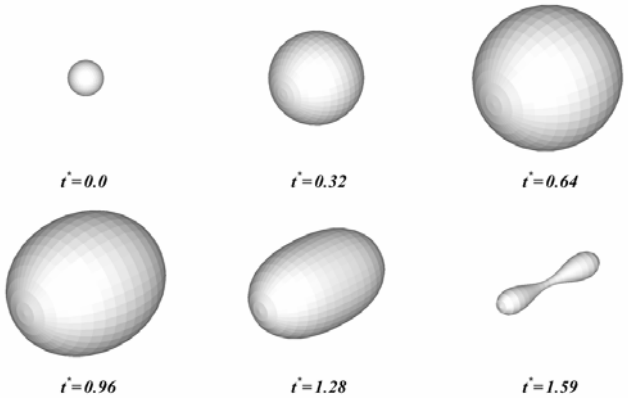

Figure 5. Bubble shape evolution in the 500ppm Polyox WSR301 solution for R_0 = 100μm. R_e=46,667, D_e=10.

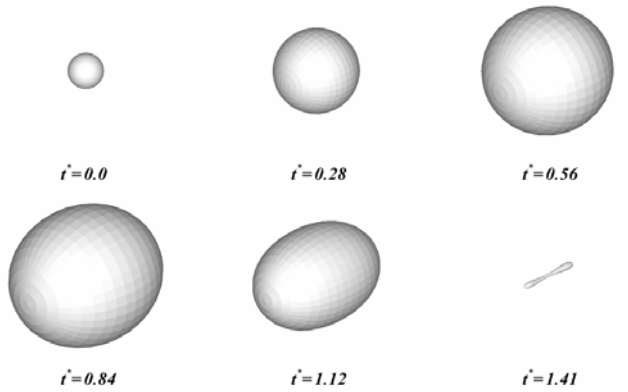

Figure 6. Bubble shape evolution in the 1,000ppm Polyox WSR301 solution for R_0 = 100μm. R_e=35,000, D_e=10.

Another major difference between water and a polymer solution is the duration for the bubble growth/collapse. The bubble period in the polymer solution is much shorter than in water. For a better comparison, the bubble radii in both a) along the vortex axis and b) in the direction perpendicular to the vortex axis, are shown versus time in Figure 8 for all three cases: water, 500ppm and 1000ppm polymer solutions. This illustrates the effect of addition of polymers on both the bubble

size (reduced by the polymer stresses) and period (shortened by the polymers).

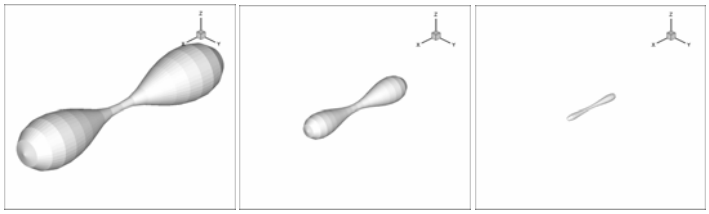

Figure 7. Final bubble size/shape comparison for: nucleus radius 100μm. From left to right, the 3 panels are for water, 500ppm and 1,000ppm Polyox solution respectively.

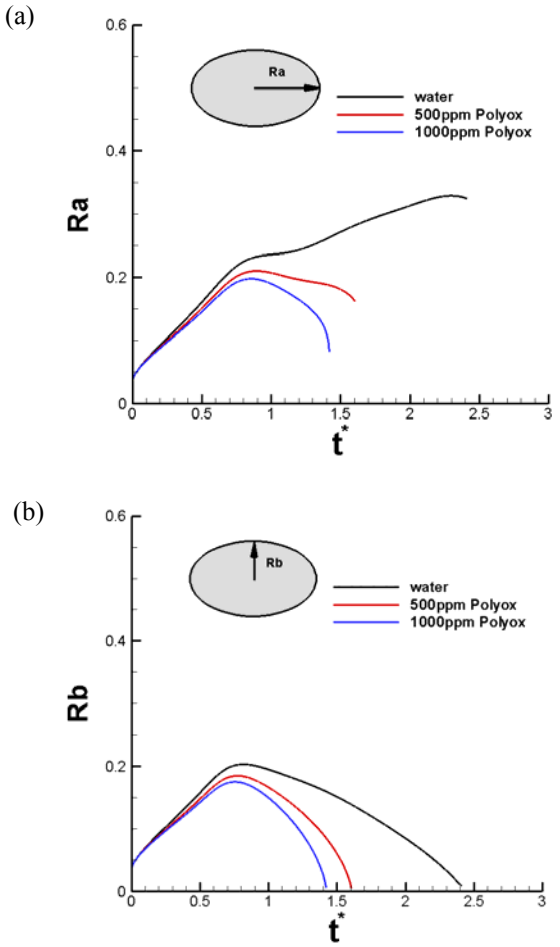

Figure 8. Bubble radii (a) along and (b) perpendicular to the vortex axis for R_0 =100μm.

Similar simulations were also carried out for a bubble nucleus of initial radius 10μm. Figure 9, Figure 10 and Figure 11 show snapshots of the bubble shape evolutions for water, 500 and 1,000ppm Polyox solutions, respectively. Different from the 100μm nucleus case, the 10μm bubble continues to elongate in water after reaching the peanut-like shape and does not collapse. The longer duration run shows that the bubble oscillates with a sausage-like shape.

For the 500ppm Polyox solution (Figure 10), the bubble behavior is quite similar to that of the 100μm nucleus. At first the bubble grows almost spherically and then shrinks and finally collapses in a spindle-like shape. However, for the 1000ppm Polyox solution, the bubble remains nearly spherical during the whole growth/collapse process.

The final bubble shapes for water, 500 and 1000ppm polymer solutions are shown in Figure 12 using the same length scale. As for the 100μm nucleus, the final bubble volume in water is much larger than those in the polymer solutions and as the concentration increases, the bubble volume decreases. Also, the duration of the growth/collapse process in water is much longer than that in a polymer solution. The bubble length along the vortex axis and radii perpendicular to the vortex axis versus time for water, 500 and 1000ppm polymer solutions are shown in Figure 13 reinforcing the above conclusions.

Seen from the results discussed above, the presence of the polymer suppresses the bubble growth. This is consistent with the experimental observation that cavitation is harder in the presence of polymers in the water. As indicated by our numerical results, a higher concentration is more efficient for the inhibition of tip vortex cavitation.

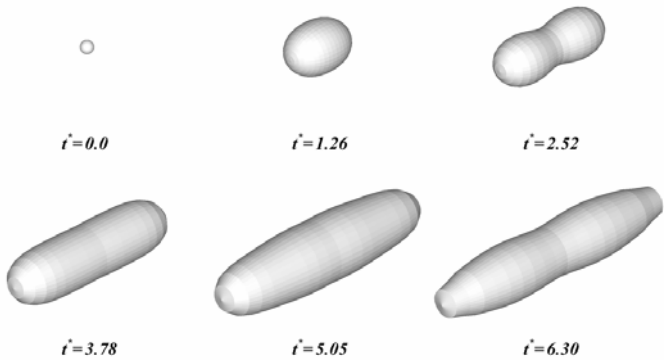

Figure 9. Bubble shape evolution in water for R_0 = 10μm, R_e=70,000.

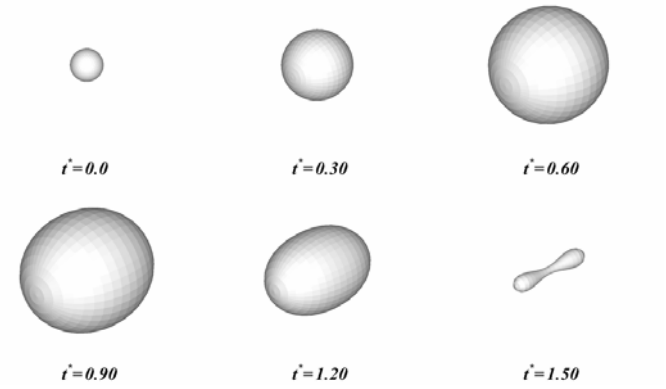

Figure 10. Bubble shape evolution in 500ppm Polyox WSR301 for R_0 = 10μm.

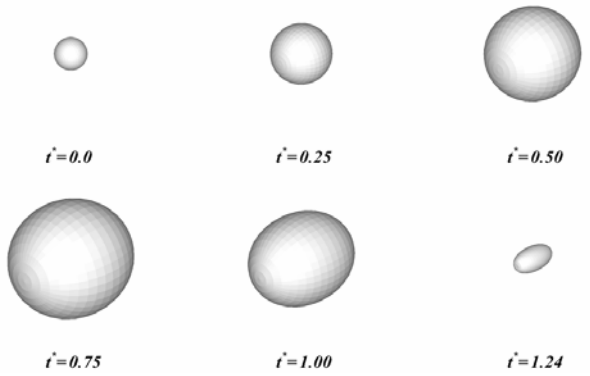

Figure 11. Bubble shape evolution in 1000ppm Polyox WSR301 for R_0 = 10μm.

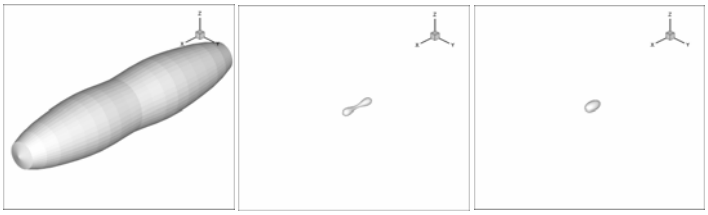

Figure 12. Final bubble size/shape comparison for a buble nucleus radius 10μm. From left to right, the 3 panels are for water, 500ppm and 1,000ppm Polyox respectively.

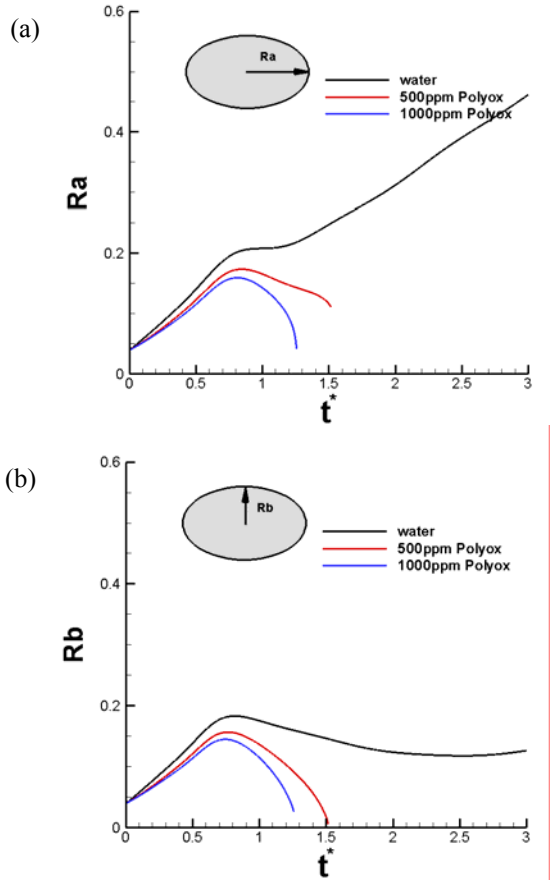

Figure 13. Bubble radii (a) along and (b) perpendicular to the vortex axis for R_0 =10μm.

Propeller tip vortex in a polymer solution

In this section, we consider the tip vortex for DTMB Propeller 5168, a five-bladed propeller with a 15.86 inch (0.40 m) diameter. The flow field around this propeller was previously simulated by Hsiao and Pauley [16]. The advance coefficient

$$J = U_\infty / nD\,, \tag{17}$$

where U_∞ is the inflow velocity, n is propeller rotational speed, and D is the propeller diameter, was chosen to be $J = 1.1$. To get a satisfactory accuracy in the solution, a RANS-DNSS approach was used [17] [18]. First, a RANS solution for the computational domain shown in Figure 14 was obtained. To improve accuracy of the solution from the RANS computations, we constructed a reduced computational domain starting from the blade tip location and which encompasses the whole tip vortex roll-up region. In this reduced domain with much finer grid , the N-S equations (for water) or Equation (2) (for polymer solutions) are solved. The details of the method can be found in Ref. [17] [18] and we briefly introduce here the procedure.

For the RANS solution, we used an H-H type grid with a total of 2.4 million points for a computational domain which was established as one blade-to-blade passage (see Figure 14). This computational domain has two side periodic boundaries, one for the suction side and one for the pressure side, formed by following the inlet flow angle. The outer boundary was located 2 propeller radii away from the hub center, while the inlet boundary was located at 1.8 propeller radii upstream and the outlet boundary was located 2 propeller radii downstream of the propeller mid-plane. The grid spacing was specified as 1.5×10^{-5} chord length near the blade surface to ensure that the first grid point is located at y^+~2. The Reynolds number defined as:

$$\mathrm{R_e} = \frac{\rho\sqrt{U_\infty^2 + (0.7\pi nD)^2}\,C_{0.7R}}{\mu}, \tag{18}$$

where $C_{0.7R}$ is propeller blade chord length at the 0.7 radius section and ν is the viscosity, was 4.19×10^{6} for water.

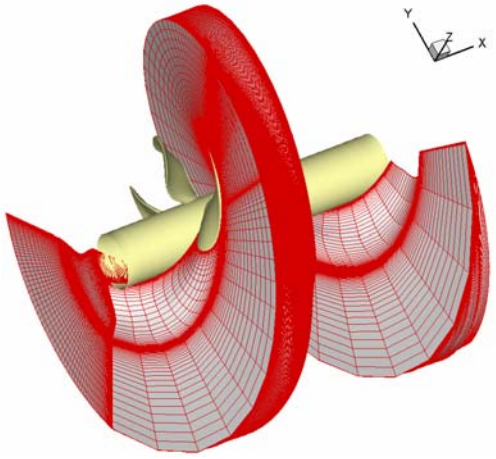

Figure 14. 3-D view of the computational grid for the RANS simulation.

The computational domain for the Direct Navier Stokes Solution (DNSS) had a square cross area and spirally extends to the end of the original RANS domain. Figure 15 illustrates the location of the reduced computational domain relative to the propeller. We considered a 7-block grid system with a total of 245 grid points in the stream wise direction and 121×121 grid points in the cross flow plane. All grid points were evenly distributed without stretching in the first five blocks but then gradually stretched out in the stream wise direction in the 6th and 7th blocks. Numerical investigations on the effect of the domain size and grid resolution were conducted to ensure that the domain and grid setup has little impact on the solutions.

For the RANS computations, all the boundary conditions were treated in an implicit manner except the outlet boundary condition. The boundary conditions on each of the boundaries are as follows: free stream conditions were specified for all variables at the inlet and outer radial boundaries; a no-slip boundary condition was applied on the blade and the hub/shaft surfaces, and a periodic boundary condition was specified on the side-boundaries. For the outlet boundary, a mass and momentum weighted extrapolation method as suggested by Chang *et al.* [17] was adopted. The velocities and pressures obtained by this method maintain proper shape of the streamlines and at the same time conserve the mass and momentum fluxes.

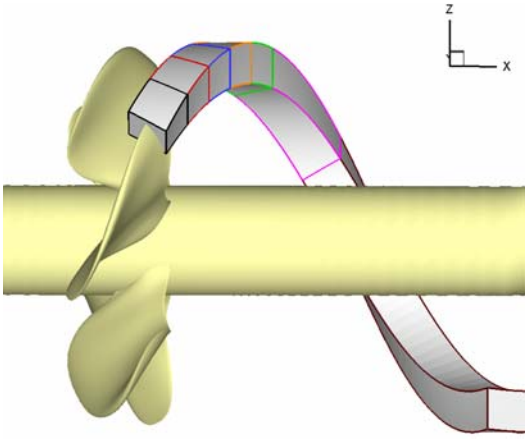

Figure 15. A view of the reduced computational domain used for the current computations.

Concentration (ppm)	*J*	R_e	D_e	β
0	1.1	4.19×10^6	0	1.00
500	1.1	2.79×10^6	0.53	0.67
1000	1.1	2.10×10^6	0.53	0.50

Table 2: Parameters used in the simulations of the propeller tip vortex.

For the reduced domain computations, the boundary conditions were deduced from the RANS solution. The initial values of the pressures and velocities interpolated from the RANS solution are imposed at all boundaries except the inlet and outlet boundaries. At the inlet boundary the method of characteristics was applied with all three components of velocities specified from the RANS solution. For the outlet boundary all the variables were extrapolated from the inner grid points. One should notice that by imposing the RANS (water) solution at the boundaries, we are imposing that the polymer effects only apply in the reduced domain, i.e. around the tip vortex centerline. This corresponds to modeling artificially the case of polymer injection from the propeller tip. The tip vortex flows for water, 500 and 1,000ppm Polyox solutions were simulated and the parameters used in the simulations are summarized in Table 2.

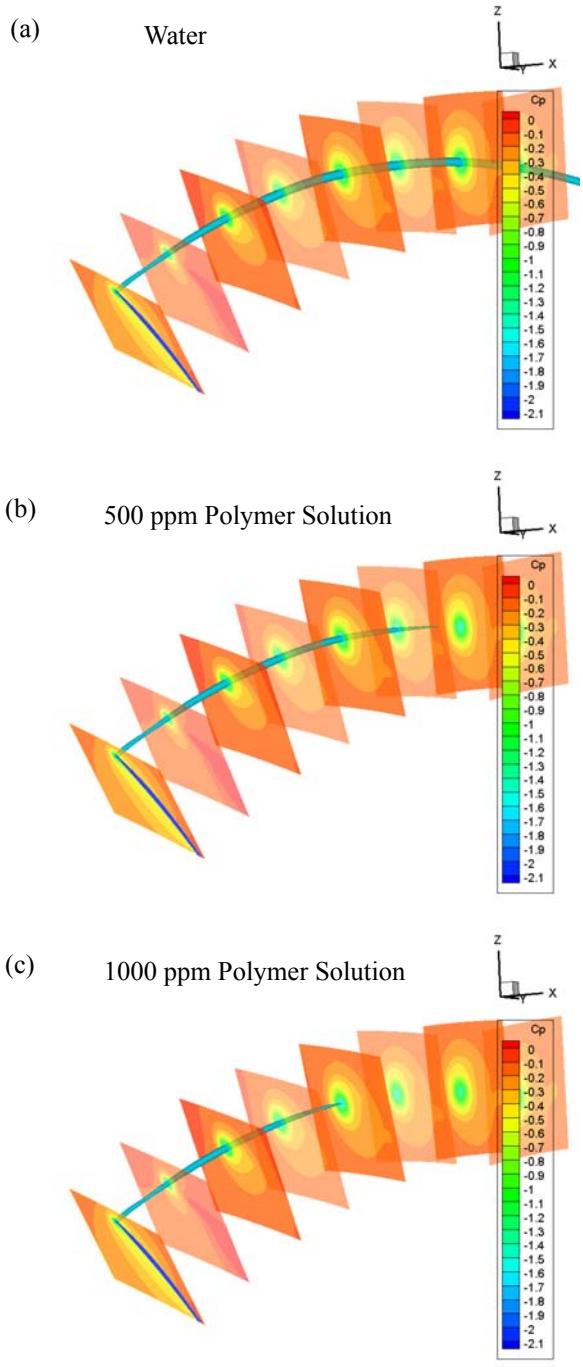

Figure 16. Iso-Cp (Cp=-1.6) surfaces equivalent to cavitation extent for (a) water, (b) 500ppm and (c) 1000ppm polymer solution.

Figure 16 shows the contours for the pressure coefficients in the tip vortex region for both a) water and b) a 500 ppm solution of Polyox and c) a 1,000 ppm solution of Polyox. As seen from the color levels, far from the vortex center (max pressure region), the pressure fields for the water and the Polyox solution are very close. However, the pressures at the vortex center are noticeably lower for water than for the Polyox solution. To illustrate the effect of the polymer solution on the cavitation shape evolution of tip vortex, the iso-Cp surface for the value of Cp corresponding to the negative cavitation number $\sigma = 1.6$ were also plotted and shown in Figure 16. This is similar to visualizing a cavitating vortex for different liquid at the same cavitation number. It is seen that for the water case a fully developed cavitation vortex core is observed to form from the tip of the blade and extend to the end of the domain. The extent of cavitating vortex become shorter as the polymer concentration is increased.

For a better comparison, the pressure coefficients along the vortex centerline are shown in Figure 17 for water, 500 ppm Polyox solution, and 1,000ppm Polyox solution. The results show that the overall pressure variations along the vortex centerline have the same trend for water and polymer solutions. In both cases, the pressure first decreases, reaches the minimum, and then increases. However, the presence of polymers makes the core pressure higher than that of water and the pressure returns faster to a higher value for a higher polymer concentration.

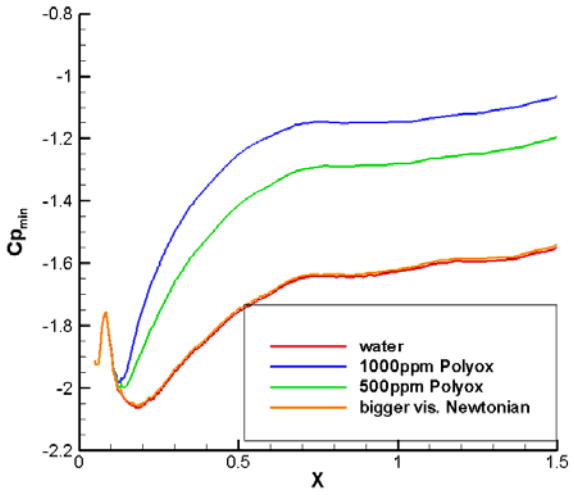

Figure 17. Comparison of the pressure coefficient variation along the vortex center. The lines in descending order are for 1000ppm Polyox, 500ppm Polyox, Newtonian fluid with a viscosity twice that of water and water, respectively.

Since the polymer solution is more viscous than water, to investigate whether the pressure rise is due to pure viscous or viscoelastic effects, we also simulated a Newtonian flow with a larger viscosity (twice that of water) and the pressure coefficient along the vortex is also shown in Figure 17. The difference between water and the twice-viscous fluid is small, indicating the strong importance of the non-Newtonian effects.

The trace of the polymer stress **T** and the pressure coefficient for the 1,000ppm Polyox solution are shown together in Figure 18. We can see that following vortex roll-up close to the propeller tip, the polymer stress dramatically increases, reaches a maximum, then decreases steadily. The same trend was also found for the 500ppm case. The fast increase of the polymer stresses correspond to stream-wise stretching of the vortex, which implies that stretch-induced normal stresses could be very important for the pressure rise.

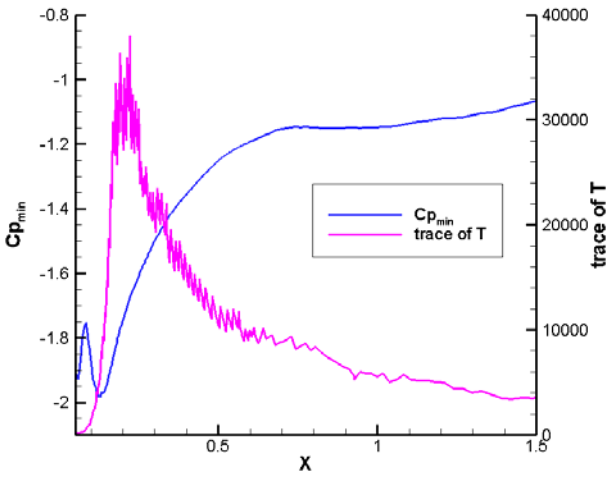

Figure 18. Pressure coefficient and the trace of polymer stress (non-dimensional) along the vortex center for the 1000ppm Polyox solution.

Figure 19 shows the maximal tangential velocity along the vortex. With polymer injected, the maximal tangential velocity becomes smaller, which is consistent with the pressure rise. The projection of the velocity along the vortex trajectory, V_s, at the vortex center is shown in Figure 20. It can be seen that the polymer injection increases this velocity component. The higher the concentration is, the more deviation from water is. This increase, however, appears to have less influence than the rotation speed on the pressure in the tip core.

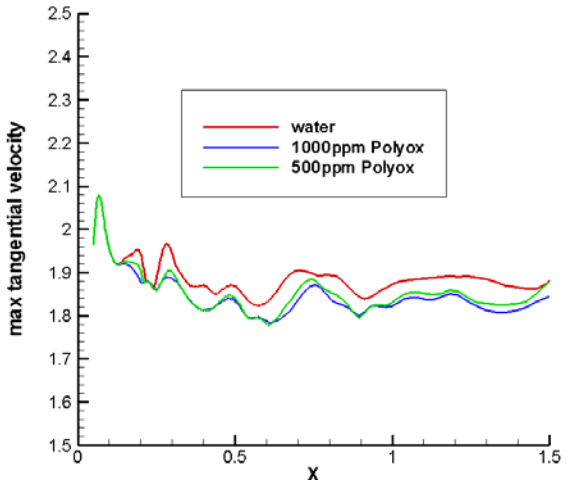

Figure 19. Maximal tangential velocity (non-dimensionalized with the free stream velocity) along the vortex.

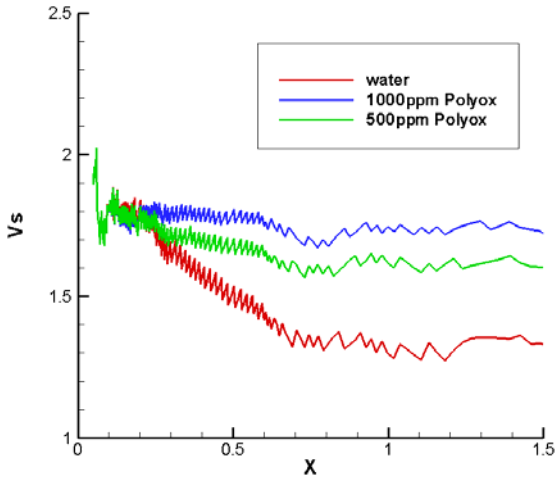

Figure 20. Velocity component parallel to the vorticity (non-dimensionalized with the free stream velocity) along the vortex center.

CONCLUSIONS

A numerical method for solving the Navier-Stokes equations was extended to allow solution of the viscoelasticity FENE-P model. With this method, numerical simulations for bubble growth and collapse in a line vortex and for propeller tip vortex flow simulations were carried out for water and polymer solutions.

Concerning the dynamics of a bubble in a line vortex, it was found that the bubbles grow more in water than in a polymer solution and this results in longer bubble periods. The polymers also inhibit bubble deformation from a spherical shape and splitting. During the growth/collapse, the bubble shapes in water and in a polymer solution are very different. In water, the bubble elongates more easily along the vortex axis, while for the polymer solutions, the bubble is prone to deform in a nearly spherical shape. These differences indicate that the presence of polymers can efficiently delay cavitation in a line vortex.

For the propeller tip vortex, polymer injection, simulated with inclusion of polymer effects only in the tip vortex centerline region, results in higher pressures at the vortex center than in pure water. The pressure along the vortex centerline was found to first decrease then increase for both water and the polymer solutions. Starting from the propeller tip, polymer stresses along the vortex centerline increase dramatically and reach a maximum in the region close to the minimum pressure point. This is a pure viscoelastic effect and was shown to not exist with a Newtonian flow with a larger viscosity. This pressure rise can explain TVC suppression with polymr injection the. These numerical results are consistent with earlier experimental observations.

In our simulations, we also found the extensibility parameter in the FENE-P affects the results quantitatively, which is a common issue for the numerical studies of viscoelastic flows (see. e.g. [6]). However, the suppression of TVC due to polymer has been confirmed in all our simulations.

ACKNOWLEDGMENTS

This work was conducted at DYNAFLOW, INC. (*www.dynaflow-inc.com*) and was supported by the Office of Naval Research under contract No. N00014-08-C-0448 monitored by Dr. Ki-Han Kim. We gratefully appreciate this support.

NOMENCLATURE

β	parameter in the FENE-P model
β_c	artificial compressibility parameter
γ	surface tension coefficient
Γ	circulation of a Rankine vortex
μ	total fluid viscosity
μ_s	solvent viscosity
μ_p	extra viscosity due to the polymer
a_c	viscous core radius for a Rankine vorex
$\mathbf{c}$	conformation tensor in the FENE-P model
$C_{0.7R}$	propeller blade chord length
D	propeller diameter
De	Deborah number
J	advanced coefficient
l	length scale
L	extensibility parameter in the FENE-P model
n	propeller rotation speed
p	pressure
R_0	initial bubble radius
Re	Reynolds number
t	time
$\mathbf{T}$	polymer stress tensor
$\mathbf{u}$	velocity vector
U	velocity scale
U_∞	propeller inlet velocity

REFERENCES

[1] Fruman, D. and Aflalo, S., "Tip Vortex Cavitation Inhibition by Drag Reducing Polymer Solution", J. Fluid Engr. 111, pp.211-216, 1989.

[2] Chahine, G.L., Frederick, G.F. and Bateman, R.D., "Propeller Tip Vortex Cavitation Suppression Using Selective Polymer Injection", J. Fluid Egnr., 115, pp.497-503, 1993.

[3] Fruman, D.H., Pichon, T. and Cerrutti, P., "Effect of a Drag-reducing Polymer Solution Ejection on Tip Vortex Cavitation", J. Mar. Sci. Tech., 1, pp.13-23, 1995.

[4] Latorre, R., Muller, A., Billard, J.Y. and Houlier, A., "Investigation of the Role of Polymer on the Delay of Tip Vortex Cavitation", J. Fluid Engr., 126, pp.724-729, 2004.

[5] Bird, R.B. Armstrong, R.C., and Hassager, O., "Dynamics of Polymeric Liquids," vol. 1&2, Wiley, New York, 1987.
[6] Li, C.F., Sureshkumar, R. and Khomami, B., "Influence of Rheological Parameters on Polymer Induced Turbulent Drag Reduction", J. Non-Newtonian Fluid Mech., 140, pp23-40, 2006.
[7] Oliveira, P.J., Pinho, F.T. and Pinto, G.A., "Numerical Simulation of Non-linear Elastic Flows with a General Collocated Finite-volume Method", J. Non-Newtonian Fluid Mech., 79, pp1-43, 1998.
[8] Chorin, A. J., "A Numerical Method for Solving Incompressible Viscous Flow Problems," Journal of Computational Physics, 2, pp. 12-26, 1967.
[9] Roe, P. L., "Approximate Riemann Solvers, Parameter Vectors, and Difference Schemes," Journal of Computational Physics, 43, pp. 357-372, 1981.
[10] Chhabra, R.P., "Drops, and Particles in Non-Newtonian Fluids", CRC Press, Boca Raton, FL, 1993.
[11] Lindner, A., Vermant, J. and Bonn, D., "How to Obtain the Elongational Viscosity of Dilute Polymer Solutions", Physica A, 319, pp.125-133, 2003.
[12] Hsiao, C.T. and Chahine, G.L., "Numerical Simulation of Bubble Dynamics in a Vortex Flow Using Navier-Stokes Computations and Moving Chimera Grid Scheme", Fourth International Symposium on Cavitation, California Institute of Technology, Pasadena, CA, June 20-23, 2001
[13] Choi, J., Hsiao, C.T., Chahine, G.L., Ceccio, "Growth Oscillation and Collapse of Vortex Cavitation Bubbles", J. Fluid Mech., 624, pp.255-279, 2009.
[14] Hsiao, C.-T., Chahine, G.L**.,** "Prediction of Vortex Cavitation Inception Using Coupled Spherical and Non-spherical Models and UnRANS Computations", 24th Symposium on Naval Hydrodynamics, Fukuoka, Japan, July 8-13, 2002.
[15] Dacles-Mariani, J., Zilliac, G.G., Chow, J.S., Bradshaw, P., "Numerical/Experimental Study of a Wingtip Vortex in the Near Field," AIAA Journal, 33, No. 9, 1995, pp.1561-1568.
[16] Hsiao, C.-T., Pauley, L. L. "Numerical Study of the Steady-State Tip Vortex Flow over a Finite-Span Hydrofoil", Journal of Fluids Engineering, 120, pp. 345-353, 1998.
[17] Hsiao, C.-T., A., Chahine, G.L., "Scaling of Tip Vortex Cavitation Inception for a Marine Open Propeller." 27th Symposium on Naval Hydrodynamics, Seoul, Korea, 5-10, Oct. 2008.
[18] Hsiao, C.-T., A., Chahine, G.L., "Numerical Study of Cavitation Inception due to Vortex/Vortex Interaction in a Ducted Propulsor" Journal of Ship Research, Vol. 52, pp. 114-123 June, 2008.
[19] Chang, J. L. C., Kwak, D., Dao, S. C., Rosen, R., "A Three-Dimensional Incompressible Flow Simulation Method and Its Application to the Space Shuttle Main Engine, Part I - Laminar Flow," AIAA Paper 85-0175, 1985.